Impact of laser powder bed fusion processing on the cyclic and fatigue properties of Ni20Cr alloy

Shubham Sanjay Joshi, Williams Lefebvre, Yan Duval, Cendrine Folton, Eric Hug, Marina Fazzini, Clément Keller

Impact of laser powder bed fusion processing on the cyclic and fatigue properties of Ni20Cr alloy

Shubham Sanjay Joshi [1], Williams Lefebvre [1], Yan Duval [1], Cendrine Folton [2], Eric Hug [2], Marina Fazzini [3], Clément Keller [3]
[1] Groupe de Physique des Matériaux, Normandie Université, INSA de Rouen Normandie, Université de Rouen, UMRCNRS 6634, Saint-Etienne du Rouvray, France
[2] Laboratoire CRISMAT, Normandie Université, Université de Caen, UMRCNRS 6508, Caen, France
[3] Laboratoire Génie de Production, INP-ENIT, Tarbes, France

Abstract: Additive manufacturing is a new-age technology specialising in intricate fabrication in the manufacturing industry. However, extremely high cooling rate and far-from-equilibrium kinetics produce heterogeneous microstructure and induce high initial dislocation density, porosity, and residual stress. These unique microstructural features are known to severely impact cyclic and fatigue properties of alloys. In such a context, we investigated the cyclic and fatigue properties of a Ni-20 wt%. Cr alloy manufactured via laser powder bed fusion process (LPBF) and compared with its cast counterpart. The fatigue testing was carried out with three different strain amplitudes depicting Low, Medium and High Cycle Fatigue (LCF, MCF, HCF). LPBF samples exhibited higher fatigue resistance than that of cast samples, however experienced early failure in all the conditions. Despite strong planar glide, LPBF samples exhibited softening behaviour; the degree of softening is similar for LCF and MCF and less pronounced for HCF. The cast samples did not undergo any softening whatsoever indicating huge differences in cyclic strain mechanisms. Masing analysis was proposed to graphically analyse this softening behaviour. Further, the flow stress was categorized into backstress and effective stress for LPBF and cast samples. Majority of softening in LPBF samples for LCF and MCF occurred via backstress, whereas effective stress is associated to HCF. To investigate the origin of this softening for LPBF samples, microstructure characterisations were performed during the softening and at fracture. Post-fatigue microstructure indicates a clear modification of the dislocation structures from those inherited from LPBF to those linked to fatigue. This gradual change in microstructure is expected to induce the cyclic softening.

Keywords: Additive manufacturing, fatigue properties, microstructure, Ni20Cr, softening behaviour, dislocations

This non edited version of the paper has been accepted for publication in Material Science and Engineering A: https://doi.org/10.1016/j.msea.2023.145915. The authors acknowledge this journal for the publication.

1. Introduction

Additive Manufacturing (AM) is a branch of techniques which enables the production of 3D parts by dividing a 3D object to 2D slices with the help of computer aided design, leading to a so-called layer by layer manufacturing [1,2]. Laser powder bed fusion (LPBF) is one leaf of this branch of AM techniques which is based on melting and rapid solidification of powder feedstock using a laser beam [1,2]. Major advantages of this technique are the flexibility of constructing intricately designed parts and adjusting microstructural features according to the required mechanical properties [3]. Rapid solidification in LPBF process strongly influences the microstructure in terms of high initial dislocation density, solute segregation, dendritic

solidification, presence of high residual stresses, distinctive meltpool features, regular or irregular shaped porosities, and stable or metastable precipitates [4]. The feedstock powder could be used in virgin state but due to high cost of powder manufacturing it is desired to re-use un-melted and un-used powder after a batch manufacturing. The reused powder can endure changes in morphology which might further induce changes in properties [5].

Commercial application of any material requires its mechanical qualification. Especially for cyclic load bearing applications, fatigue performance is of utmost importance. LPBF process enhances mechanical strength in tension or compression for several material systems with respect to their cast or wrought counterparts [6]. Nevertheless, it lowers the fatigue strength compared to their conventionally manufactured counterparts, probably due to the defects induced by LPBF. Indeed, the aforementioned defects formed during LPBF process especially pores [7], surface roughness [8], Lack Of Fusion (LOFs) [9] can impact fatigue performance of parts manufactured via LPBF to a greater extent, much more significant than in simple loading [10]. Hence it is important to investigate the influence of such microstructure with defects on fatigue performance. Firstly, Witkin et al. concluded that higher degree of surface roughness is one of the most significant factor to hamper the fatigue life of AM samples [11]. Secondly, many papers discussed the High Cycle Fatigue (HCF) behaviour of materials fabricated via LPBF, such as 304L SS [12], 316L [13], Al-Mg alloys [14], Ti-6Al-4V [15], Inconel 718 [11] and many more, helping to understand the fracture mechanisms in HCF for LPBF materials [13,16]. This HCF behaviour is also affected by the powder reusing as reported for IN718 [17]. Such a behaviour in several LPBF materials could occur due to an increase in particle size diameter [7] with recycling associated to larger amount of porosities [7], surface roughness [8] and oxidation [18].

Nevertheless, when it comes to Low Cycle Fatigue (LCF), the number of published articles is much lower that than for HCF despite similar importance (thermal fatigue, accidental fatigue loading…). Regarding LCF, several studies pointed out cyclic softening experienced by LPBF materials when high degree of plasticity is involved. Specifically LPBF Inconel 718 [17,19], CrMnFeCoNi high entropy alloy [20], Ti-alloy [21], 316L SS [22] among several studies experience cyclic softening for higher strain amplitudes. Surprisingly, this feature seems to be independent of the material suggesting similar softening mechanisms which still have to be understood for LPBF materials.

Cyclic softening or hardening in conventionally manufactured alloys has been studied extensively in the past century making a clear connection between softening/hardening and chemical or microstructural material characteristics such as stacking fault energy (SFE), initial microstructure, dislocations, loading characteristics, temperature etc. [23–26]. SFE is one of the most important criteria to predict cyclic hardening or softening to accommodate the plastic strain [27]. Alloys with high SFE are prone to deformation via cross slip, which also leads to dislocation cell structures. Copper, which is prone to cross slip [27], experiences cyclic softening due to decrement in dislocation density by dislocation annihilation [28]. Besides, when alloyed with Al, Cu exhibits lowered SFE, reducing, in turn, cyclic softening [27] which has been also observed for other planar glide materials [23,29]. On the other hand, the mechanical loading can also affect the cyclic softening which starts for microplastic cyclic loading for cross-slip materials whereas full plastic loading is needed to induce softening for planar glide materials [23,29]. The aforementioned general softening reported of LPBF materials in LCF conditions seems, hence, to contradict the observations reported for cast. The objective of our work is, thus, to better understand the strain mechanisms for LPBF materials

subjected to different plastic cyclic loadings, with, it particular, the origin of the softening behaviour in low cycle fatigue. Ni20Cr was selected to investigate this cyclic behaviour.

This material has two main advantages: i) it is a monophasic and almost precipitate-free material even with LPBF manufacturing [3] with model strain mechanisms and ii) it has low SFE and pronounced planar glide tendency [30,31] which is supposed to restrict cross-slip and cyclic softening. Besides, Ni20Cr is widely employed industrially amongst several available Ni-Cr binary alloys with applications in electro-mechanical systems like actuators and sensors due to excellent mechanical properties and electrical resistance at high temperature and strong corrosion resistance [32]. Presently all these applications are being fulfilled by the conventionally produced Ni20Cr by single roll strip casting, continuous casting [33]. Good solubility of Cr in Ni and declivity of the formation of intermetallic phases in this alloy, enable good creep resistance [34]. A few works have studied Ni20Cr alloy produced by additive manufacturing [3,30] investigating parameter optimization for densely manufactured specimens, microstructural analysis, tensile properties, however, the issue of cyclic and fatigue behaviour has never been addressed in the literature. For thorough investigation of fatigue properties of Ni20Cr fabricated via LPBF, following questions must be answered:

- Do LPBF Ni20Cr samples show different fatigue response from that of cast Ni20Cr?
- Is there any cyclic hardening/ softening involved during fatigue testing of LPBF Ni20Cr? and if yes then which microstructural features are influencing it?

This research looks at the deformation mechanisms in cyclic testing of LPBF specimens and how they differ from cast specimens. The specimens were machined for this purpose in order to "eliminate" some initial surface effects, and tests were performed at room temperature. The objectives of this paper are then to provide answers to these novel questions using fatigue testing and dislocation structures characterisation.

2. Materials and methods

2.1. Sample fabrication

The samples were produced under Argon protective gas using an SLM125^{HL} machine equipped with a 400 W Yb fibre laser. The parameter set provided in table 1 of the paper was adapted from a previously published study that considered an array of various process parameters [30]. The parameters were chosen based on the fabrication of specimens with nearly fully dense sample (greater than 99.8%). Furthermore, these parameters were chosen because as they do not result in a strong crystallographic and morphological texture, meaning to reduce mechanical anisotropy. The build-plate contained cubic samples (measuring 20×20×20 mm^3) and cylindrical samples (100 mm in height and 10 mm in radius) oriented alongside the building direction. The cubic samples were used for porosity analysis. The cylindrical samples were machined (to avoid surface roughness issues of as-built LPBF samples) to produce dog-bone specimens with a uniform gauge section designed for fatigue testing according to the ISO-12106:2017 standard (gauge diameter of 8 mm and gauge length of 20 mm).

Table 1: Optimized parameters used for LPBF fabrication of Ni20Cr specimens.

LPBF parameters	Data
laser power (*P*)	200 W
scanning speed (*v*)	900 mm/s
hatch distance (*h*)	0.12 mm
layer thickness (*t*)	30 µm
scanning strategy	Stripes (rotation angle of 67°)

The pre-alloyed powder was provided by Höganäs AB and two powder feedstocks were employed, one with the as-received powder (labelled AR in this work) and a second one which experienced 33 production cycles (also called reused powder labelled as RU). Inductively Coupled Plasma Optical Emission Spectrometry (ICP-OES) was used to determine the chemical composition of the as-received powder (table 2). Instrumental Gas Analysis (IGA) determined an oxygen content of 264 ppm (±4 ppm) [30].

Table 2: Chemical composition of the powder as measured by ICP-EOS in weight percent. Each element's detection errors are shown in brackets.

Cr	Fe	Si	Mn	Al	Ni
19.9 (0.1)	0.0222 (0.0002)	0.035 (0.001)	<0.0002	0.047 (0.001)	Balance

Fig. 1(a)-(b) illustrate the morphology and size distribution of the as-received powder, respectively. Particles are mostly spherical with some elongated ones, as well as the presence of satellites. In volume fraction, the size distribution is Gaussian with an average powder particle value of about 30 µm. LPBF samples fabricated with AR and RU powder will also be addressed as AR samples and RU samples.

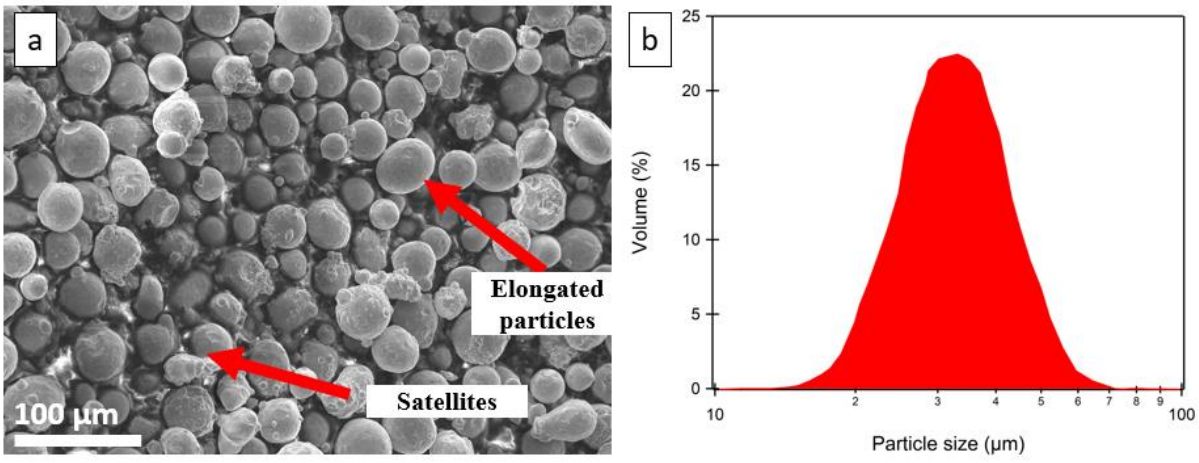

Figure 1: (a) SEM micrograph of as-received powder particles of Ni20Cr particles and (b) powder diameter distribution.

For fatigue behaviour comparison purpose, dog-bone cast Ni20Cr samples were obtained commercially according to the same dimensions as the ISO-12106:2017 standard. These samples were cold drawn, machined according to the aforementioned standard and finally homogenized at their solutionizing temperature of 1150 °C for 10h.

2.2. Microstructural analysis

For microstructure investigation, a JEOL 7900F Scanning Electron Microscope (SEM) equipped with Secondary Electron (SE) detector, Electron Back-Scattered Detector (EBSD), and Energy Dispersive X-Ray Spectroscopy (EDS) detector was employed. A JEOL ARM Scanning Transmission Electron Microscope (STEM) was also used for high magnification analyses.

For SEM observations, the samples were exposed to metallographic preparation starting from mechanical grinding and polishing using SiC abrasive papers followed by electropolishing in a Struers A2 electrolyte at 15 V for 30 s. A step size of 1 µm alongside with a 5° misorientation criteria was employed for the EBSD analysis for grain boundary detection. Dislocations were also imaged at low magnification using SEM and Electron Channelling Contrast Imaging (ECCI) technique. Those analysis were performed at an 8 mm working distance with an acceleration voltage of 25 V associated to an electron current of 8-12 nA (read using Probe current detector) associated to an emission current of 102.4 µA.

For STEM analysis, thin slices of 500 µm were cut using precision cutting machine and were mechanically ground using SiC paper up to grit size 2400 until a thickness of 100 µm was obtained. Then thin discs of 3 mm in diameter were extracted using a punch hole device, followed by electropolishing using Struers TenuPol-5 (jet polishing system) with a 90% methanol and 10% perchloric acid electrolyte at 24 V and -40 °C. Electron transparency can be achieved in the thin discs using this step via hole formation. Finally, Gatan precision ion polishing system (PIPS-2) was employed for post processing of electropolished discs intended to prepare plain-view thin areas subsequent to the hole for better characterisation. The milling parameters selected were 0.5 eV energy with milling angles of ± 3°. The acceleration voltage of the JEOL ARM 200F used in this study in bright field scanning transmission electron microscopy (BF STEM) mode was 200 kV.

2.3. Cyclic stress-strain and fatigue testing

LPBF and cast Ni20Cr samples were subjected to two different cyclic mechanical loadings. First, Cyclic Stress-Strain Curves (CSSC) were acquired for total strain amplitudes ranging from 2.5×10^{-4} to 10^{-2} mm/mm (strain-controlled full reversed conditions: strain ratio R=-1) with an increment of 2.5×10^{-4} after every 200 cycles. Maximum and minimum values of stresses and strains are obtained using this test which is used to calculate mean stress, stress and strain amplitudes and further plastic strain amplitudes. The purpose of CSSC is to rapidly classify the cyclic behaviour of a material over an extensive region of plastic strain amplitudes [17]. Based on these tests, three different zones of plastic strain amplitudes of 5×10^{-3}, 5×10^{-4}, and 5×10^{-5} mm/mm respectively were identified and further categorized as Low Cycle Fatigue (LCF), Medium Cycle Fatigue (MCF), High Cycle Fatigue (HCF). Those plastic strain amplitudes were then employed to carry out pure fatigue tests in strain control mode (strain ratio R=-1) for both AM and cast samples. As reused powder may affect the fatigue properties of LPBF alloys [17], samples manufactured from the two powder batches will be analysed separately. Both the CSSC

and fatigue tests were performed on MTS servo-hydraulic machine with a load capacity of 100 kN in with the help of a "clip-on" extensometer with the strain limit of 0.15. Three samples were employed for CSSC and fatigue tests for both kinds of powder manufacturing routes to achieve statistically representative data.

2.4. Cottrell's method for stress partioning

Flow stress during cyclic test can be partitioned into effective stress (σ_{eff}) and back stress (X) components which are associated to isotropic and kinematic hardening, respectively. They can be calculated by inspecting the reversal yield point σ_r associated to the yield surface either in loading or unloading sequence of the hysteresis loop. In that case, following literature, the effective stress and backstress can be computed using equations (1) and (2), in the order given. To that aim, σ_r was determined using plastic strain offset of 2×10^{-5} [23], which is a value in agreement with the extensometer sensibility. σ_{min} and σ_{max} are the minimum and maximum stresses associated to a fatigue sequence.

$$\sigma_{eff} = \frac{(\sigma_{max} - \sigma_r)}{2} \quad (1)$$

$$X = \sigma_{max} - \sigma_{eff} \quad (2)$$

The two stress components are illustrated in fig. 2 during the loading and unloading sequences. The effective stress is associated to the radius of the yield surface (i.e., elastic domain) and the backstress is related to the centre of this yield surface in the stress space.

The backstress being anisotropic by nature [23,35], for cycling loadings, a mean backstress and a backstress amplitude can be defined using the X values characterized in the loading and unloading part of the stress-strain loop. Backstress can be associated to kinematic hardening or softening related to long range microstructural interactions between mobile dislocations and grain boundaries, dendrite walls, heterogeneous dislocation structures. The effective stress associated to isotropic hardening or softening is linked to short range microstructural interactions between mobile dislocations and coherent precipitates, and forest dislocations. X_a is the amplitude of back stress which can be computed by eq. 3.

$$X_a = \frac{X_+ + |X_-|}{2} \quad (3)$$

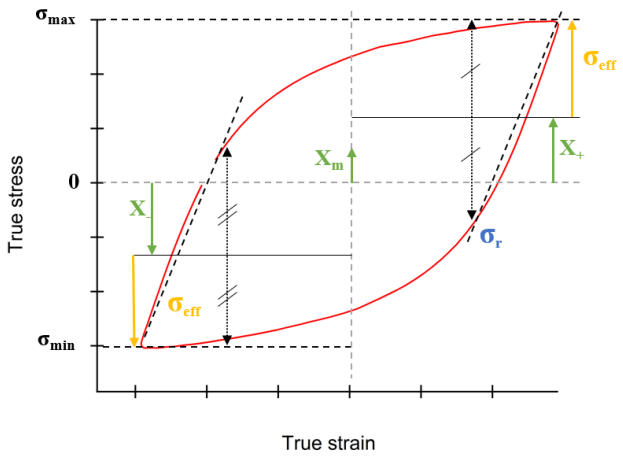

Figure 2: Illustration of a cycle and flow stress partitioning.

2.5. Masing analysis

The cyclic behaviour of materials influences the shape and type of stress-strain hysteresis loops of fatigue testing [36–39]. Following previous research [40–46] and recently reviewed by Yadav et al. [36], these loops can be further divided into two categories as Masing and non-Masing [36,37]. Masing analysis is done by superimposing the minimum true stress-strain points of all selected hysteresis curves at the same origin in order to compare the cyclic hardening among cycle number increment. Masing behaviour can be explained as superimposition of hysteresis curves for different cycles with geometrical similarity [36,44]. On the contrary, non-Masing behaviour can be connected to no-superimposition obtained by cyclic hardening or softening [42,44]. Non-Masing behaviour is generally associated to a change in microstructure [39,42].

3. Results

3.1. Initial microstructural investigation

First of all, no major microstructural differences were observed in terms of dendritic structures, dislocations, grain size or texture intensities for LPBF specimens fabricated using the two powder feedstocks. Hence, the following microstructure characterisation is presented without any mention of the associated powder feedstock.

A first overview of microstructure of LPBF and cast Ni20Cr can be seen via SEM in fig. 3(a)-(f). The LPBF micrograph planes are parallel to the building direction (YZ plane) of fabrication in fig. 3(a)-(b); fig. 3(a) indicates the presence of melting pools with fine grains, whereas fig. 3(b) shows a colony of dendritic cellular structures. In fig. 3(b), such a colony of dendritic cells drawn using "hyphen-lines" is shown and red mark specifies the presence of oxides (white spots) formed during the LPBF samples, over these dendrites. Fig. 3(c)-(d) are the micrographs of plane normal to the building direction (cross section- XY direction) of LPBF Ni20Cr specimens. Fig. 3(c) shows the presence of typical dendritic cells going in the plane as a colony of cellular dendrites, and fig. 3 (d) indicates the presence of heterogeneously formed dislocation structures associated to these cellular structures. The average primary arm spacing (λ) was calculated to be 0.47±0.05 µm (95% of confidence index) considering several different colonies of dendritic cells. The cell size is associated to the average cooling rate ($\dot{T}$) involved during the fabrication process and was calculated to be about $\mathbf{(2.78\pm0.85)\times10^{6}}$ $K.s^{-1}$ using eq. 4 for Ni alloys [47], in agreement with literature [30].

$$\lambda = 97\dot{T}^{-0.36} \quad (4)$$

Fig. 3(e)-(f) depict cast Ni20Cr microstructure with huge grains as well as dislocations and dendrite-free matrix due to complete homogenized setting after heating over recrystallization temperature.

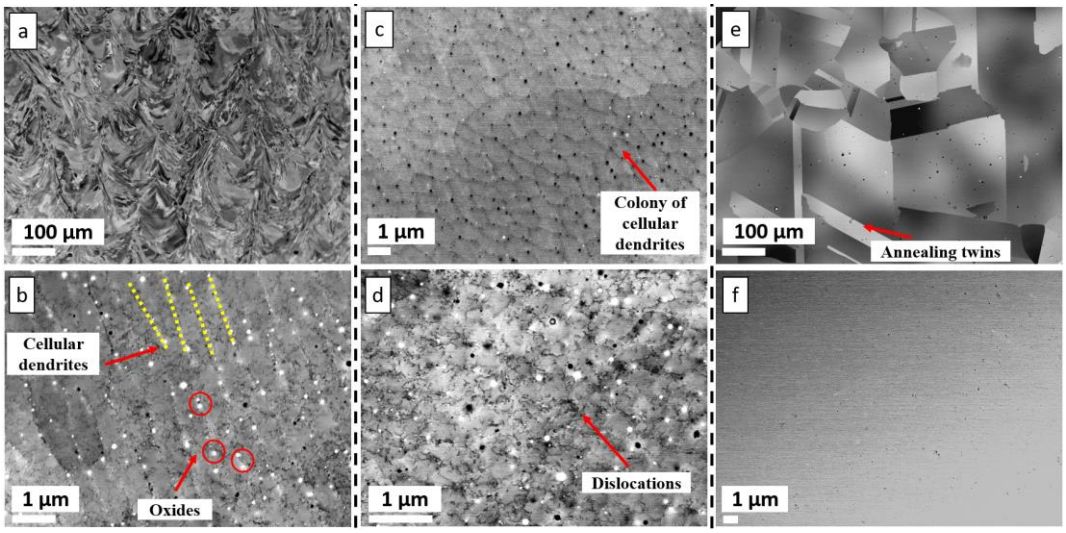

Figure 3: SEM observation of: (a) general initial grain structure for LPBF in YZ plane, (b) cellular dendritic structures for LPBF in YZ plane, (c) a colony of cellular dendrites for LPBF in XY plane, (d) dislocation structures for LPBF in XY plane, (e) general initial grain structure for cast samples and (f) initial dislocation free microstructure of cast Ni20Cr.

3.2. Cyclic stress-strain curve analysis

CSSC tests were performed on LPBF and cast Ni20Cr samples, where they were subjected to alternating symmetrical tension and compression cycles as described earlier. The strain levels varied from 2.5×10^{-4} to 10^{-2} (mm/mm) (fully reversed condition) with an augmentation of 2.5×10^{-4} after every 200 cycles. Completely different mechanical response was recorded for LPBF and cast specimens as can be seen in fig. 4. LPBF specimens attain high values of stress amplitude indicating higher cyclic hardening at the beginning of plasticity but tend to saturate with higher amplitudes. Besides, no effect of the employed powder batch is observed in that case. For cast specimens, related cyclic hardening associated to stress amplitude is comparatively low but increases parabolically with increasing plastic strain amplitudes. Based on these tests, the three different plastic strain amplitudes of 5×10^{-3}, 5×10^{-4}, and 5×10^{-5} (mm/mm) respectively were categorized as LCF, MCF, HCF and marked using grey hyphen-lines in fig. 4. The subsequent total strain amplitude values employed for these tests are given in table 3 considering average values of Young's modulus of 219 GPa (LPBF) and 190 GPa (cast) obtained from the cyclic loops.

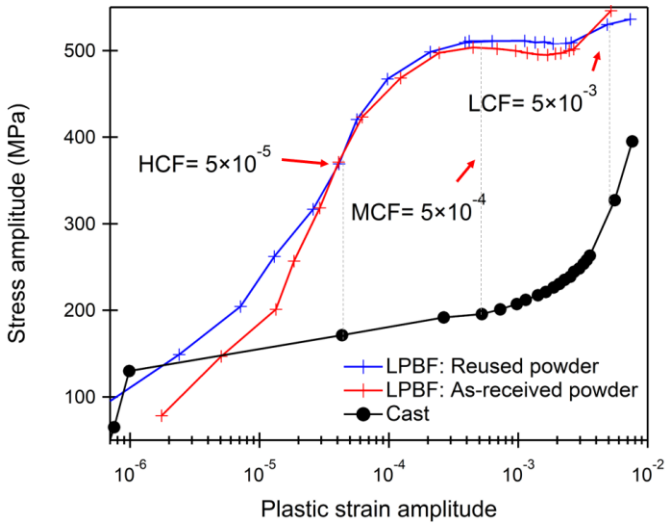

Figure 4: Cyclic stress-strain curve for LPBF and cast samples.

Table 3: Estimation of total strain amplitude for fatigue tests.

3.3. Fatigue testing

In order to compare the fatigue behaviour between all LPBF and cast samples, similar average plastic strain amplitudes must be ensured. As fatigue test are controlled in total strain amplitude, the average values of the plastic strain amplitude for LPBF specimens fabricated using the two powder batches AR and RU (red and blue markers) and cast Ni20Cr specimens (black markers), as provided in fig. 5 as a function of the cycle to failure. This figure shows slight variation in plastic strain amplitude for the different testing conditions owing to difference in elastic modulus, residual stress, dislocation density of LPBF and cast specimens. Nevertheless, for a given fatigue condition (LCF, MCF, HCF), those variations are of a second order compared to the one between each testing conditions and assumed not to influence the fatigue behaviour. Consequently, for each fatigue condition, a clear comparison between all samples can be done.

Type	Total strain amplitude for LPBF	Total strain amplitude for cast	Plastic strain amplitude
High Cycle	1.97×10^{-3}	-	5×10^{-5}
Medium Cycle	2.84×10^{-3}	1.48×10^{-3}	5×10^{-4}
Low Cycle	7.43×10^{-3}	5.84×10^{-3}	5×10^{-3}

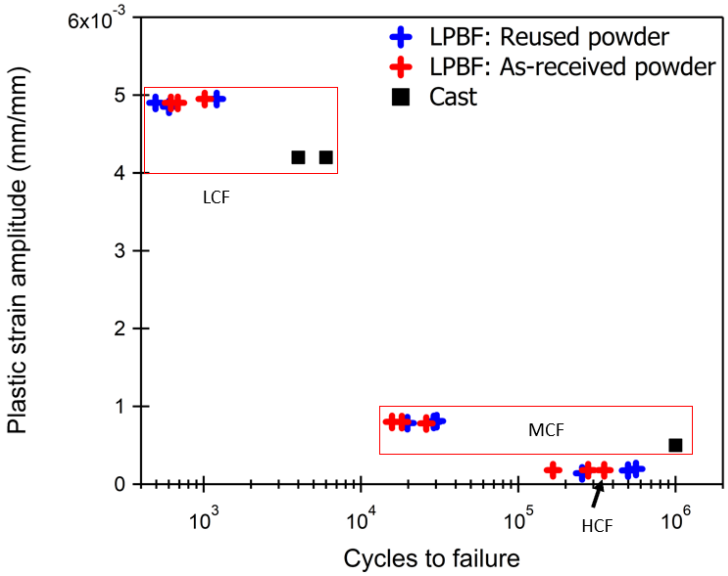

Figure 5: Plastic strain amplitudes versus cycles to failure for LPBF and cast Ni20Cr samples.

Fig. 6 depicts the evolution of the stress amplitude with respect to the number of cycles for all specimens. After achieving an accurate control of the test (a few tens of cycles for LCF and a few hundreds of cycles for MCF), LPBF (both AR and RU) specimens experience similar softening behaviour for LCF and MCF. In particular, it can be observed in fig. 6 that LCF fatigue curves are prolongated by MCF ones. On the contrary, cast Ni20Cr specimens did not experience any softening in LCF and MCF conditions.

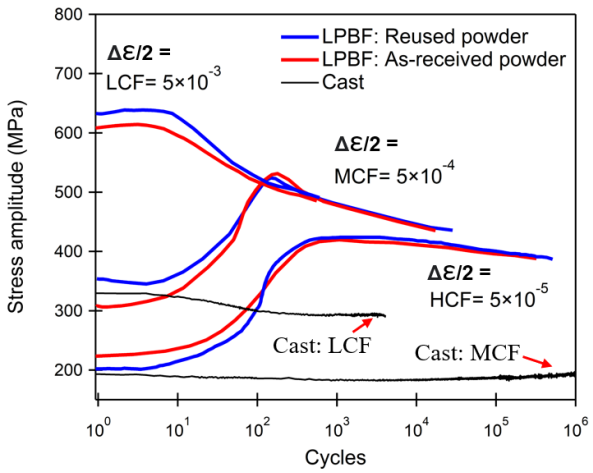

Figure 6: Evolution of stress amplitudes for LPBF and cast Ni20Cr samples for the three fatigue conditions (LCF, MCF and HCF). For each condition, plastic strain amplitude is indicated along the curves.

No significant difference was observed in stress amplitude evolution between LPBF samples fabricated using the two powder batches, in agreement with the similar microstructure obtained from these two powders.

Table 4: Average stress amplitudes and cycles to failure for LPBF and cast Ni20Cr for different fatigue tests.

Average stress amplitude (in MPa)			
Test type	LPBF: Reused	LPBF: As-received	Cast
LCF	516 ± 11.2	504 ± 4	315 ± 1.4
MCF	451 ± 4	446 ± 6.2	188 ± 2
HCF	400 ± 2.8	400 ± 3.6	Not performed

LPBF specimens of Ni20Cr, irrespective of the employed powder batch, showed higher fatigue strength than that of cast specimens as shown in fig. 7. LPBF specimens (average from all curves) showed approximately 510 MPa fatigue strength for LCF against 315 MPa for cast Ni20Cr. Cast specimens showed an average fatigue life of 5275 cycles which was significantly higher than that for LPBF samples (770 cycles). For MCF condition, LPBF Ni20Cr specimens exhibit the same trend seen in LCF, with higher fatigue strength of approximately 448 MPa against 188 MPa for cast specimens. These cast specimens show great fatigue resistance as none of the samples failed at 1 million cycles whereas LPBF specimens depicted an average fatigue life of approximately 26000 cycles for this MCF conditions. LPBF shows as high as 400 MPa fatigue strength for HCF, whereas cast samples were not tested in HCF conditions as these samples did not even fail after 1 million cycles at relatively higher plastic strain in MCF. Despite similar machining conditions, those results reveal that LPBF samples display a fatigue life one order of magnitude lower than cast for a given fatigue loading conditions. This difference is much more pronounced than the one reported for 316L for instance [22].

LPBF reused (RU) specimens showed slightly higher fatigue strength of 516 MPa against specimens fabricated with the as-received (AR) specimens of 504 MPa as seen in table 4, whereas average lifetime was similar with close to 770 cycles. For MCF, fatigue resistance was comparable for both kinds of specimens with 451 MPa for RU samples and 446 MPa for AR specimens, but differences were seen in fatigue lifetime as summarized in table 5. RU specimens failed after an average number of 26385 cycles which is slightly higher than for AR specimens with 19986 cycles. For HCF, no difference was found in the average stress amplitude value for samples produced using the two powder batches, but fatigue life for RU based specimens was significantly higher (438502 cycles) than the one for AR specimens (266670 cycles). The associated standard deviation values for stresses and cycles to failure are seen in the table 4. The effect of powder reusing on the fatigue life in HCF conditions seems to be consistent with previous works [17,22]. In the case of Ni20Cr, this increase by an almost factor close to two of the fatigue life for reused powder is the opposite of the one reported for other material such as IN718 [17]. However, the large experimental scattering on the number of cycles at fracture does not enable any definitive conclusion regarding the effect of powder reusing on fatigue which is analogous to the findings of Berez et al. arguing no impact of powder recycling (reusing) on fatigue behaviour of 17-4 Stainless Steel [48].

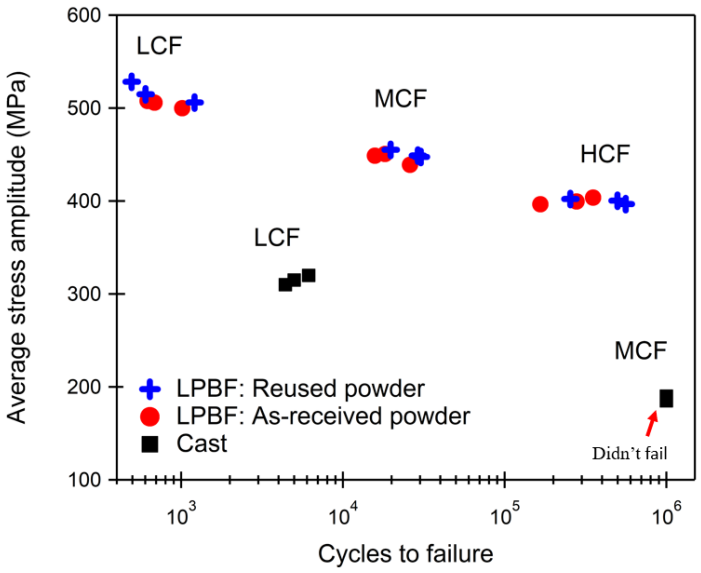

Figure 7: Average stress amplitudes for LPBF compared to cast Ni20Cr.

Table 5: Cycles to failure for different types of Ni20Cr samples at different testing conditions.

	Plastic strain amplitude	LPBF RU samples	LPBF AR samples	Cast samples
Low cycle	5×10^{-3}	769 ± 350	770 ± 200	5275 ± 1000
Medium cycle	5×10^{-4}	26385 ± 5500	19986 ± 5000	>1 million* (*samples didn't fail)
High cycle	5×10^{-5}	438502 ± 150000	265670 ± 90000	-

In order to investigate the origin of the fatigue life differences between both kinds of LPBF samples in HCF loading condition, fracture surfaces were observed by SEM. It could be noted that the fully reversed fatigue tests tend to flatten the fracture surface during compression. This could happen as the sample might experience some tension and compression cycle even after failure and this makes the analysis more difficult. Fig. 8(a)-(f) illustrates those fracture surfaces features of both kinds of LPBF specimens fabricated via the as-received and the reused powder batches in HCF. Fig. 8(a) illustrates the fracture surface of RU specimens divided into two major zones labelled 1 and 2, those zones being magnified in Fig. 8(b)-(c), respectively. Fig. 8(b) illustrates typical striations related to fatigue crack propagation for zone 1, whereas flake or flaky structures are observed in Fig. 8(c). The zones with striations can be seen in homogeneous and extended stretches and cover a larger area than zone 2. For AR samples, fig. 8(d) indicates a similar overview of the fracture surface. Fig. 8(e) shows the magnified zone 1 with striations whereas fig. 8(f) indicates zone 2 of fracture surface which contains fine dimples arranged parallelly. The size of these dimples was estimated to be close to 0.5 µm which corresponds to the size of cellular dendrites as marked by yellow indicators. These fracture characteristics for both samples seem to indicate similar fatigue damage with zone 1 associated to crack propagation and zone 2 related to sudden ductile fracture.

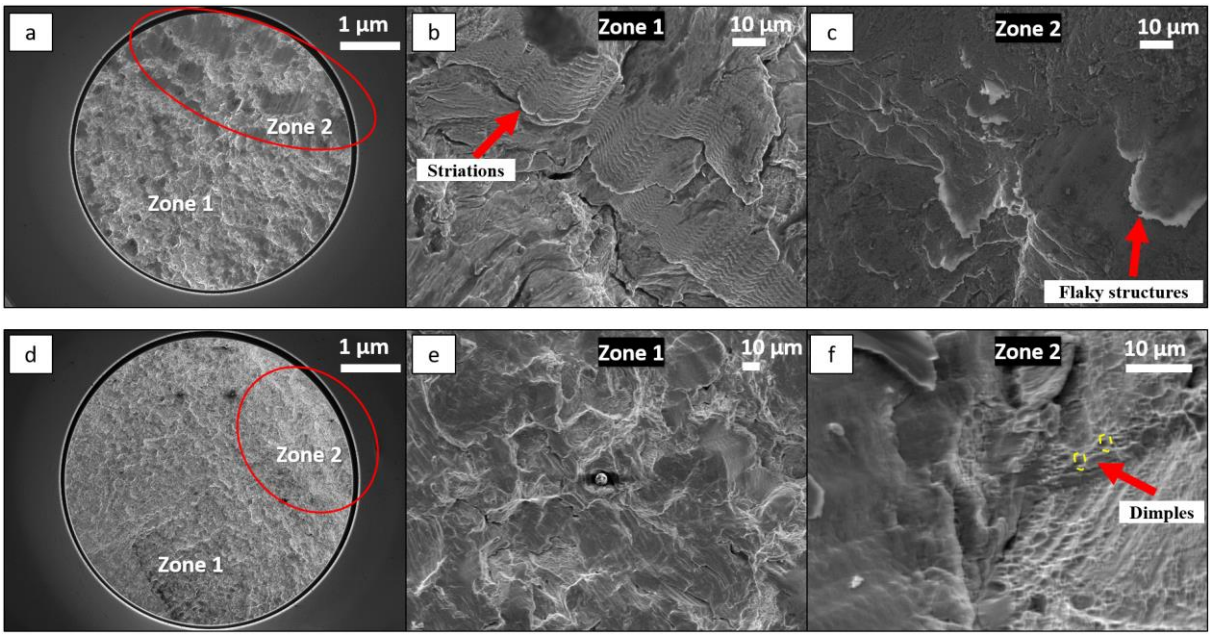

Figure 8: SEM observations of: (a) larger view of fracture surface of high cycle fatigue of reused powder specimen using SEM; (b) magnified zone 1 showing striations; (c) magnified zone 2 with flakes; d) fracture surface of high cycle fatigued as-received powder specimen; (e) striations in magnified 'zone 1' and (f) parallel strips of ductile dimples in magnified zone 2 of as-received powder LPBF specimen.

3.4. Masing analysis

Masing analysis of the fatigue data is reported in fig. 9(a)-(e). The objective of performing Masing analysis is to investigate the softening/hardening behaviour of different types of Ni20Cr samples. As shown in previous section (fig. 6), no difference was found in softening behaviour of reused and as-received powder LPBF specimens. Hence this analysis is focused on the difference in softening behaviour of LPBF and cast samples. The LPBF specimens selected for analysis here are fabricated by reused powder as they shown longer fatigue life. Fig. 9(a)-(b) indicate Masing plots in LCF conditions for LPBF and cast Ni20Cr, respectively. Cast Ni20Cr specify Masing behaviour which can be explained as superimposition of hysteresis curves for different cycles with geometrical similarity [36,44], as shown by the circle with superimposition in fig. 9(b) and fig. 9(d). This indicates that cast Ni20Cr specimens did not undergo any softening already seen in the stress amplitude evolution plot. On the contrary, in LCF conditions, LPBF specimens undergo softening with stress reduction of approximately 165 MPa and the plots for LPBF can be categorized as non-Masing behaviour [49,50] (no master curve). This softening can be connected to changes in microstructure from one cycle to another.

Fig. 9(c)-(d) depict Masing plots of LBPF and cast Ni20Cr specimens for MCF conditions and similar results are reported as LCF. Indeed, LPBF specimens show non-Masing behaviour with stress reduction of approximately 105 MPa. Cast specimens depict perfect Masing behaviour subsequently with stable microstructure as the specimens do not fail until 10^6 cycles.

LPBF specimens undergo softening indicating non-Masing behaviour for HCF as can be seen in Fig. 9(e). The stress reduction was observed to be close to 29 MPa. Cast specimens were not tested in HCF condition as these samples did not fail even for MCF condition.

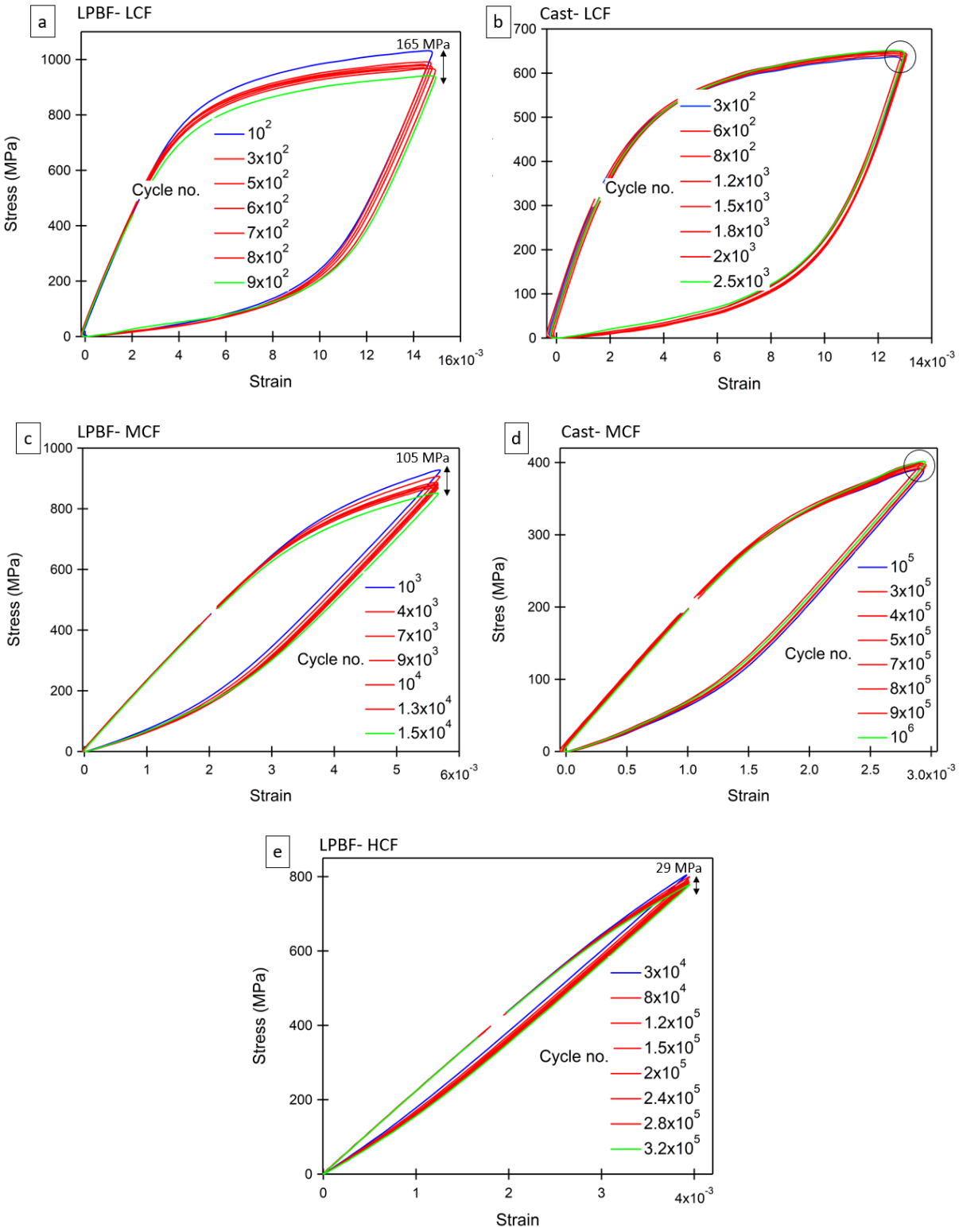

Figure 9: Masing plots indicating selected fatigue cycles of: (a)-(c)-(e) LPBF samples produced using reused powder cycled in LCF, MCF and HCF conditions, respectively and (b)-(d) Cast samples cycles in LCF and MCF conditions, in the order given.

3.5. Stress partitioning

In order to better understand the microstructure modifications suggested by Masing plots for LPBF samples, the backstress amplitude (X_a) (eq. 3) and the effective stress (σ_{eff}) (eq. 1) evolutions as a number of cycles are plotted in fig. 10. In these two figures, LPBF and cast samples as well as for the three fatigue conditions are plotted. Moreover, in this figure, solid lines mark the evolution of respective parameters when the applied strain amplitude correspond to the desired one. On the contrary, markers of different shapes are associated to data during strain amplitude control adjusting. LPBF specimens show similar softening behaviour qualitatively in LCF and MCF conditions and lower degree of softening rate seen in HCF. Nevertheless, the comparison of effective stress and backstress evolutions reveals that the softening is mainly due to the backstress amplitude. Indeed, in the case of LPBF-LCF, the total stress amplitude reduction is close to 165 MPa (see fig. 9(a)) with about 140 MPa backstress amplitude reduction versus 25 MPa for the effective stress. For LPBF-MCF specimens, backstress amplitude reduction accounts upto 80 MPa, whereas effective stress reduction is approximately 25 MPa. No evolution of backstress was observed for LPBF-HCF specimens as well as cast specimens for LCF and MCF conditions. All these values are presented in table 6.

Table 6: Average value of flow stress, effective stress and backstress reduction for LPBF Ni20Cr samples tested in LCF, MCF and HCF. Data are related to reused powder specimens.

	Total stress reduction (MPa)	Effective stress reduction (MPa)	Back stress reduction (MPa)
Low cycle	165	25	140
Medium cycle	105	25	80
High cycle	29	29	0

Stress reduction observed for LPBF-HCF was close to 29 MPa, also computed via Masing analysis and can be connected to effective stress (σ_{eff}) revealing a similar softening for this stress component for all fatigue tests. Cast specimens for LCF and MCF conditions indicate no stress reduction confirming no softening behaviour. This connection of softening behaviour with flow stress components is directly linked with microstructure and will be discussed in detail in the further sections.

It could be noted that the average effective stress value for LPBF samples subjected to fatigue tests is in agreement with the value reported in tension [24], revealing the similar short-range interactions of mobile dislocations with the microstructure for both kind of mechanical loadings.

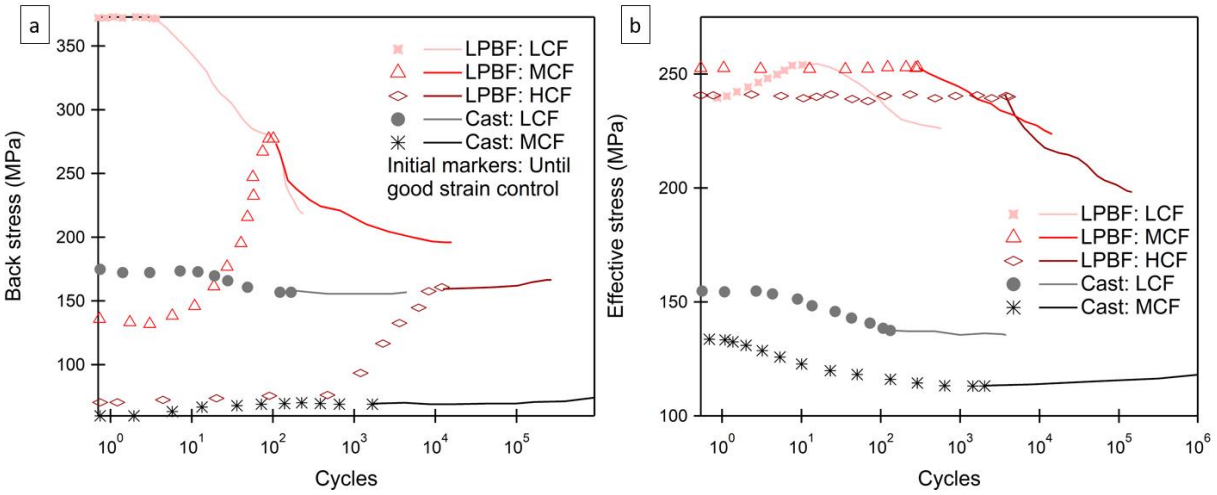

Figure 10: Evolution of the stress components versus the number of cycles for: (a) back stress for LPBF and cast Ni20Cr samples at different fatigue testing conditions. Markers illustrate the behaviour before the achievement of the desired total strain.

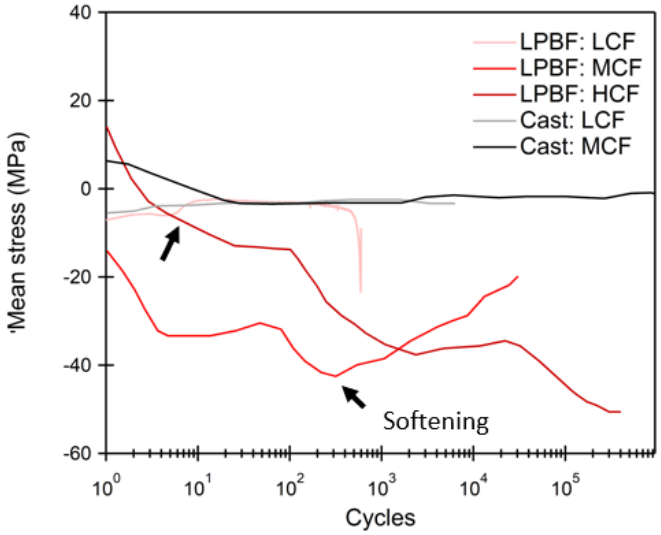

Figure 11: Evolution of mean stress against cycles for LPBF (RP) and Cast Ni20Cr samples at different fatigue testing conditions.

It is interesting to note that the onset of softening in all the three conditions can be associated with the modification of mean stress. Fig. 11 shows that for LPBF-LCF the existing negative mean stress starts to modify at the onset of softening (10 cycles) and attains zero mean stress value. For LPBF-MCF, mean stress value modifies just after 100 cycles which is the onset of softening. For LPBF-HCF, no softening of average stress was observed. It could be noted that, as expected due to their fully recrystallized character and no residual stresses, cast samples present an average stress close to zero.

3.6. Post fatigue-microstructural characterisation

ECCI-SEM observations on post-fatigued LPBF (RU) samples can be seen in fig. 12-13. In LCF conditions (fig. 12), at low magnification, dislocation cells seem to be modified with respect to the one observed in the as-built state (fig. 3(d)). First, slip bands, indicated by bordered yellow lines and arrows in fig. 12(a) are observed, suggesting strain localisation. Then,

fig. 12(b), which magnifies the centre of fig. 12(a), illustrates different changes in the dislocation structure with respect to the as-built state. On one hand, an area between the two slip bands with a reduced dislocation density is observed, could be indicated by softened zone. On the other hand, inside the slip bands, new dislocation structures are observed. These new dislocation walls are no longer associated to former dendrites. Compared to the as-built state, those walls are thicker and, curved similarly to mobile dislocations observed in this figure. This reveals the role played by plasticity on those new dislocation walls.

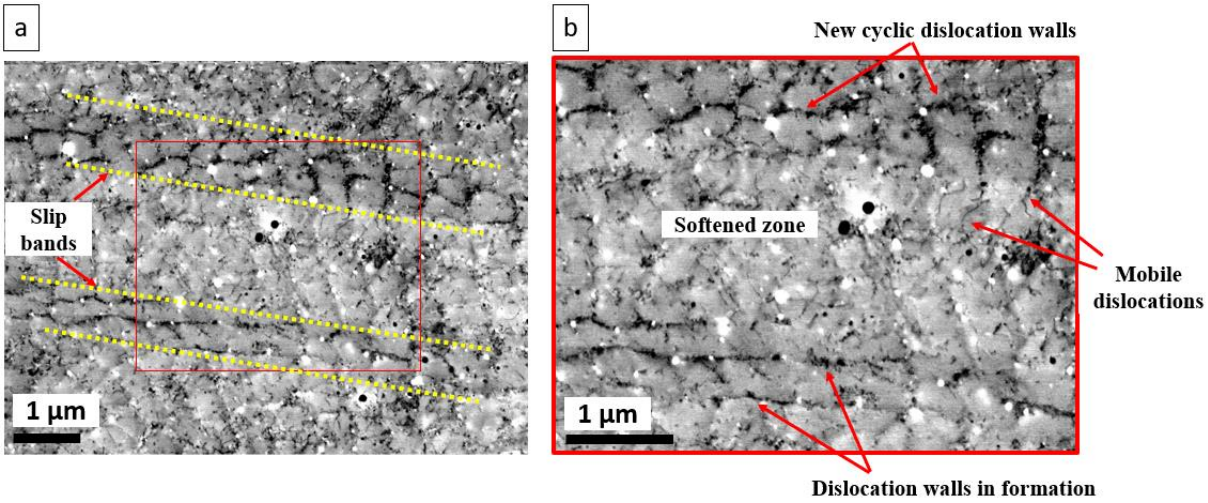

Figure 12: ECCI-SEM based imaging of post fatigued LPBF in LCF indicating: (a) slip bands and (b) magnified image of yellow box in (a) indicating modified dislocation structures.

Fig. 13(a)-(b) indicate the micrograph for LPBF samples tested in MCF and HCF condition, respectively. In fig. 13(a) a softened zone is observed as for LCF condition with some thick dislocation walls without well-defined new dislocation structures as for LCF. For HCF conditions (fig.13(b)), no significant dislocation structure modification is observed with respect to the as-built state (see fig. 3(d)).

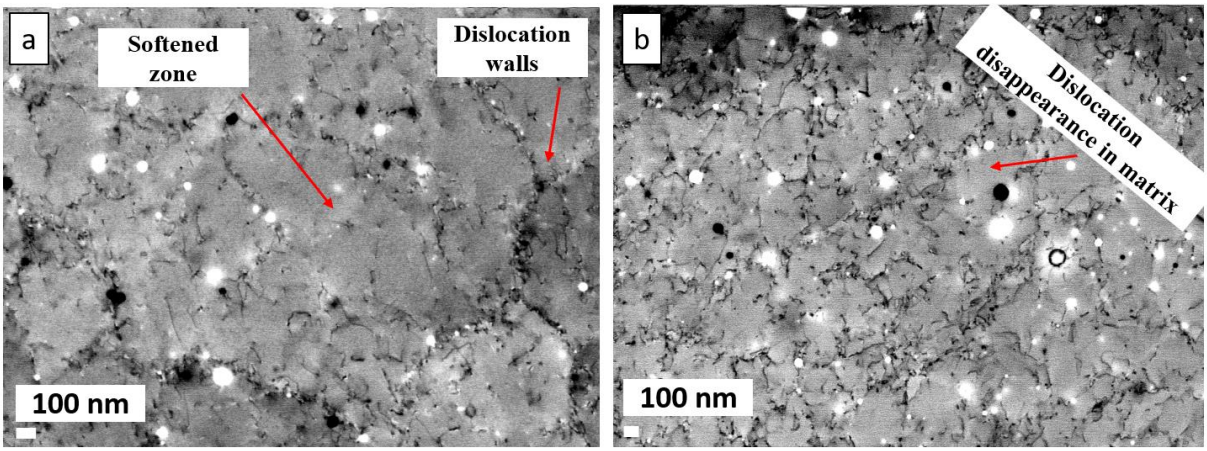

Figure 13: ECCI-SEM based imaging of post fatigued LPBF: (a) MCF conditions and, (b) HCF conditions.

4. Discussion

The results described above reveal strong differences in cyclic and fatigue behaviour between Ni20Cr manufactured conventionally and by LPBF. In the following paragraphs, the effect of the LPBF defects on fatigue and the origin of cyclic softening are discussed.

4.1. Effect of defects and powder reusing on fatigue properties

LPBF specimens manufactured using the as-received and reused powder feedstock show an array of similar microstructural features (grain size, dendrite size, texture…). For LCF and MCF, significant plasticity occurs during the fatigue tests and, in that case, fatigue life is associated to microstructural defects such as dislocation density or heterogeneous dislocation structures [51,52]. As no initial dislocation structure differences were evidenced between the samples produced using the two powder batches, fatigue life is similar for both kind of samples, as observed in literature for IN718 [17] and 316L [22].

For HCF, fatigue life is affected by surface or sub-surface defects and porosities [8,18]. Following literature [53], the probable sources of formation of pores found in LPBF samples correctly manufactured (i.e., conduction mode with enough volumetric energy) and no keyhole formation are i) pores entrapped in feedstock powder as seen in for aluminium alloys [54] and steels [55] and ii) voids between powder particles in the powder bed as seen, for instance, for Ti64 alloy [56,57] and for Al-Si-Mg system [58]. Prithivirajan *et. al*. mentioned the critical size of porosity to be 20 µm to influence crack nucleation close to the pore in additively manufactured Inconel 718 [59]. Besides, the inter-pore distance was also mentioned to play a role on the fatigue life [53,59] especially when this value is about the order of magnitude of the pore size [53]. Following fatigue data presented in the previous section, all samples (cast, AR and RU LPBF) may differ by the number and size of porosities larger than 20 µm.

In order to focus on the porosity distribution for both kind of samples, complementary X-ray tomography analysis of the gauge length of two samples fractured in HCF conditions (AR and RU) was conducted. Analysed samples were chosen in order to maximize their difference in fatigue lives (AR sample failed at 250000 cycles whereas RU ones failed at 450000 cycles). RX solution tomograph working at 150kV was employed. The voxel size was about 8x8x8 µm. First, a similar value of relative density of about 99.99% for both samples revealing very high dense samples. Then, fig. 14(a)-(b) illustrate the reconstructed volume of the AR and RU specimens, respectively. The top of the images represents the fractured areas.

In both cases, pores are observed in the analysed volume. Far from the fracture surface, the pore distribution seems to be uniform in the volume. In the case of fig. 14(b), a crack which did not propagate is observed. From those observations, the pore size distributions were computed for both samples and compared in fig. 15 inside the volume under the fracture surface (depicted with a blue rectangle). Note that the unpropagated crack was removed from the analysis of the RU sample.

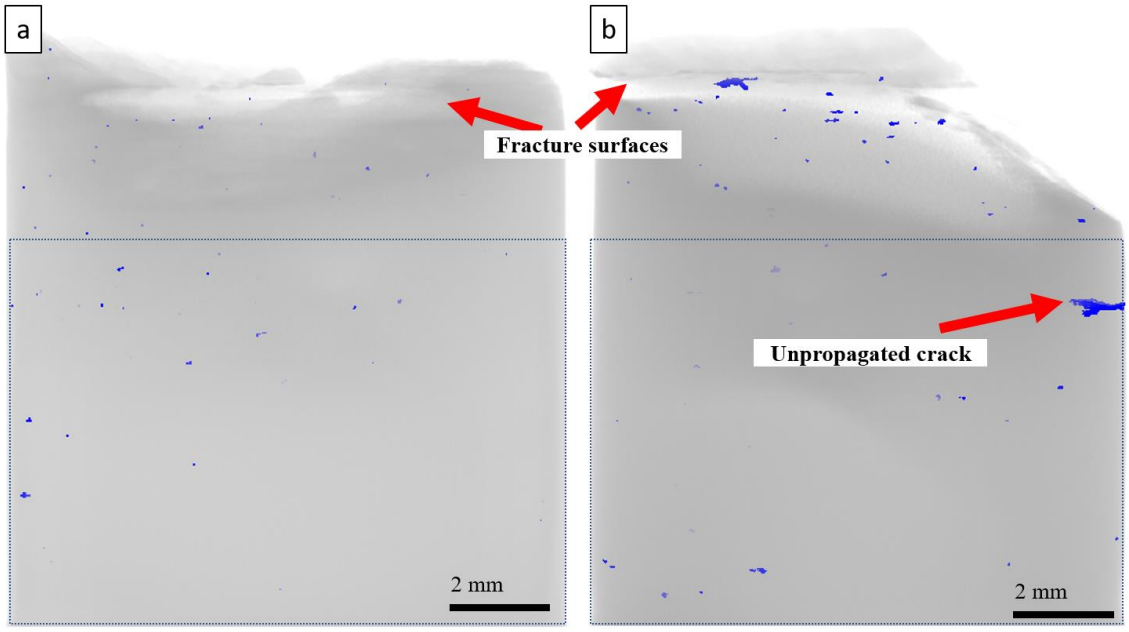

Figure 14: X-ray tomography reconstructed volume for: (a) as-received powder and (b) reused powder. Porosities are highlighted in semi-transparency in blue. Blue rectangle depicts the volume considered for porosity statistics analysis.

Based on fig. 15 examination, similar pore distributions are observed with pore diameter (assuming spherical morphology) ranging between 7 and 50 µm with slightly larger pores for RU compared to AR. On one hand, this significant number of pores with diameters larger than 20 µm well explains the low fatigue lives of both AR and RU samples manufactured using LPBF compared to cast reported in table 4. On the other hand, those results cannot explain the slight difference in fatigue lives in HCF conditions between samples manufactured using as-received and reused powder batches. Consequently, it is believed that in the case of Ni20Cr, powder reusing (in the range of production number considered in this study) does not affect the fatigue life. Irrespective of the powder employed, LPBF samples indicate significantly larger pores despite employing optimised process parameters than that of in cast samples, hence the fatigue life is lower in LPBF samples.

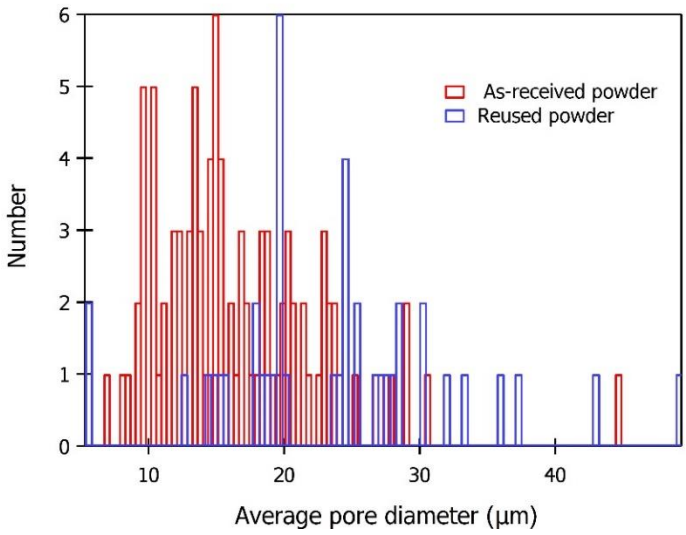

Figure 15: Comparison of the pore size distribution obtained by X-ray tomography between samples manufactured with the as-received and reused powder batches.

It should be noted that, in the case of HCF, residual stresses are still present in the sample (inherited from the LPBF process and modified by the machining process) and observed on the surface of LPBF alloys [60,61]. Such residual stresses may also participate in the early of fatigue damage compared to cast. This is not the case for LCF as residual stresses are erased during the cyclic loading (mean stress close to zero value, as seen in fig. 11).

4.2. Origin of softening in LPBF Ni20Cr

LPBF specimens underwent softening in all the conditions of LCF, MCF and HCF. Specimens in LCF and MCF experienced comparable slopes of softening with much reduced slope in HCF. In literature, cyclic softening is associated to cross slip activation which leads to dislocation annihilation and a gradual change in dislocation structures [39,62]. Considering the strong planar glide character of the Ni20Cr, cyclic softening for AM samples is then unexpected.

The non-Masing behaviour for LPBF Ni20Cr specimens subjected to all fatigue conditions suggests a change in microstructure during those fatigue tests. This change in microstructure is confirmed by the dislocation structure characterisation by both ECCI (see fig. 12 and 13) which illustrates that the initial dislocation cells associated to dendrites are replaced by new heterogeneous structures for LCF and MCF conditions as well as matrix areas with reduced dislocation density (i.e. dislocation density in soft zones) for all fatigue loadings.

This two-fold microstructure modification explains first the effective stress softening observed in the results section. This stress component is related to short-range interactions of mobile dislocation with forest dislocations or small-size coherent precipitates (oxides). Following literature [24,63], the effective stress can be expressed as follows:

$$\sigma_{eff.} = \sigma_{s.s.} + \alpha M \mu b \sqrt{\rho_s} \quad (5)$$

In that equation, $\sigma_{s.s.}$ represents the solid solution contribution to the effective stress, M is the Taylor factor, μ is the shear modulus, b is the magnitude of the Burger's vector and α is a parameter averaging the strength of the different dislocation to dislocation interactions. The qualitative decrease in dislocation density in soft zones ρ_s characterised in the results section associated to eq. 5, confirm the effective stress softening observed macroscopically.

Secondly, the presence of pronounced change in dislocation structures over slip bands (fig. 12(a)-(b)) modify both the size of the dislocation structures as well as the dislocation density in hard zones and the volume fraction associated to these hard zones. As for effective stress, it has been proved that the backstress (X) can be expressed, in first approximation, as a function of microstructure features following eq. 6 [24].

$$X = \frac{k_{HP}}{\sqrt{d}} + f_g K_s \frac{\mu b M}{l_0} \quad (6)$$

Here, the first term of the right-hand side of the eq. 6 is related to the contribution of the average grain size d associated to the Hall-Petch coefficient K_{HP} whereas the second term is linked to the contribution of the heterogeneous dislocation structures of average size (l_0) with volume fraction of grains including such dislocation structures (f_g) and K_s is a material parameter. As a result of the slip bands, the size and shape of dislocation structures are changed explaining the softening of the backstress. Assuming that the grain size contribution to backstress is constant during the fatigue test and using the μ, b, M, K_s and fg parameters reported for LPBF Ni20Cr in a previous study [24], the backstress softening characterized for LCF conditions (i.e. 140

MPa) is supposed to induce an increase in average dimensions of the dislocation structures from 0.47 µm (initial value, see section 3.1) roughly to 0.9 µm. This value seems to be qualitatively in agreement with the observation of ECCI images of the post-fatigue dislocation structures. A proper computation of this post fatigue dislocation structure size should be performed to conclude on this point.

Besides, it could be noted that this backstress softening only appears for MCF and LCF conditions with a higher intensity for the latter condition. This indicates association of cyclic softening behaviour with plastic strain amplitude. In particular, backstress softening is triggered by a threshold value probably between that of MCF and HCF. To investigate this threshold value without performing several fatigue tests, raw data which was employed to plot the CSSC curves, can be studied in detail. Fig. 16(a) depicts the evolution of stress amplitude versus the number of cycles of LPBF specimen during a CSSC test. Hardening and eventually saturation is seen till 2200 cycles with no softening during each applied cyclic sequence, whereas fig. 16(b), which is the magnified zone of fig. 16(a), depicts a clear inception of softening at 2400 cycles. This softening is expected to be associated to backstress amplitude as effective stress softening should not be significant during a CSSC sequence of 200 cycles.

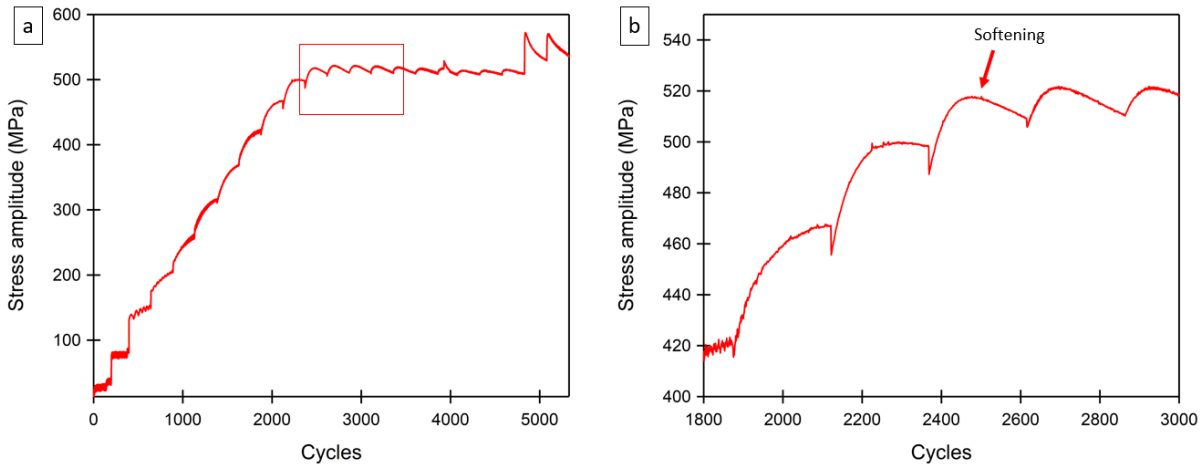

Figure 16: (a) Stress amplitude against number of cycles for Cyclic Stress-Strain Curve analysis of LPBF samples; and (b) magnified zones of '(a)' as marked in red.

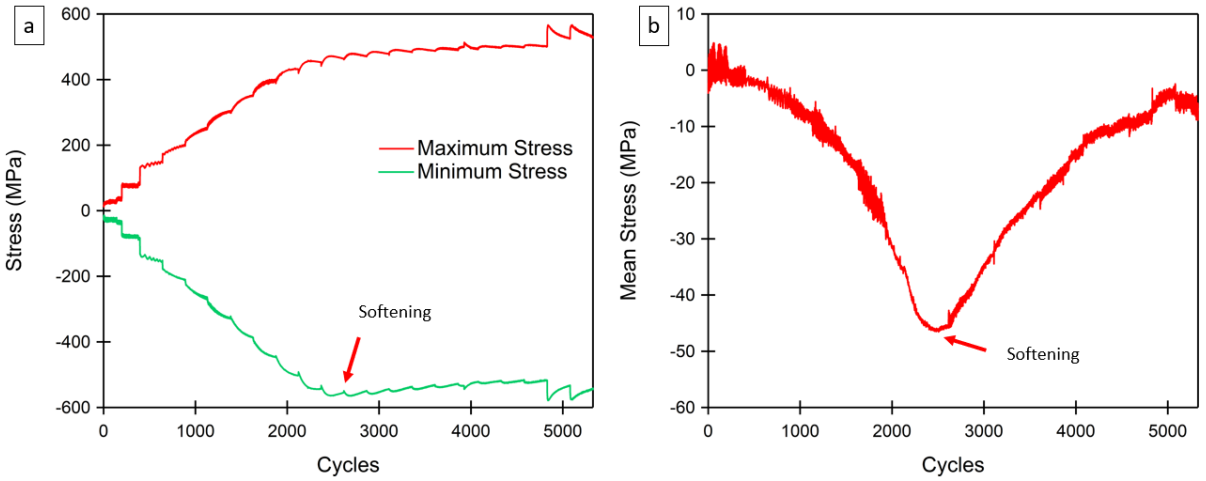

Figure 17: (a) Evolution of minimum and maximum stress against number of cycles of LPBF samples; and (b) Mean stress against number of cycles for Cyclic Stress-Strain Curve analysis.

This softening of the stress amplitude affects both maximal and minimal stress as illustrated in fig. 17(a). Nevertheless, it can be observed that the cumulative softening in all successive cyclic sequences is more important for the minimal stress for which the stress is decreasing during each sequence but also from a sequence to another whereas maximal stress is rather constant from one sequence to another as soon as softening started. As a consequence of this asymmetrical softening, the mean stress is also reduced after 2400 cycles as illustrated in fig. 17(b).

Maximal stress at which the softening begins is found to be 470 MPa associated to a plastic strain amplitude of about 10^{-4}, lower than the one applied in MCF fatigue tests. This plastic strain amplitude corresponds to microplasticity and to a stress of about 0.85 of the macroscopical yield stress in tension (554 MPa) [24]. For a cast sample exhibiting initial dislocation structures introduced by tensile loading, this ratio is about 0.98 [27], suggesting that dislocation structures inherited from AM (LPBF) are less stable than those inherited from an initial mechanical loading.

As cross slip is restricted for Ni20Cr, the initiation of softening for stresses below the macroscopical yield stress indicates an early local activation of slip systems which alter the initial microstructure. To confirm this mechanism, complementary TEM analysis of MCF-LPBF specimen interrupted at 1000 cycles has been conducted. This point is associated the softening phenomenon occurring during a fatigue test (MCF). Fig. 18(a) illustrates the activation of one slip system in microplasticity regime (plastic strain amplitude of 5×10^{-4}). To better understand the origin of such slip system activation, fig. 18(b) magnifies the location of the expected initiation of plastic slip for the activated slip system observed on the right part of the fig. 18(a). Red circle in fig. 18(b) marks a dislocation segment pinned by two nanoscale precipitates or oxides (indicated with red arrows) which can probably act as a dislocation source for plastic slip inception. It is hence believed that dendrite walls associated to a high dislocation density and nano-sized precipitates can lead to early slip activation. Once activated, those activated slip systems may start to induce a change in dislocation structures and, then, may localize the plastic deformation in slip bands as observed for LCF conditions, leading, in turn, to cyclic softening.

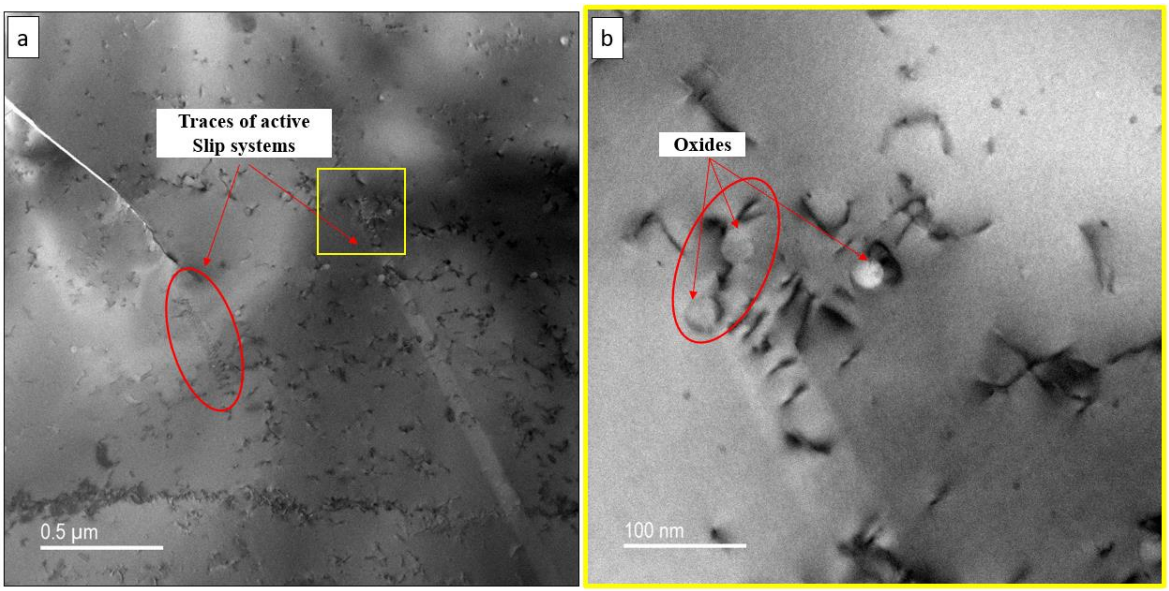

Figure 18: (a) and (b) Bright field STEM analysis of LPBF sample with medium cycle fatigue stopped after 1000 cycles indicating possible dislocation pile ups and oxides interacting with dislocations.

5. Conclusions

In this investigation, the cyclic and fatigue behaviour of Ni20Cr alloy fabricated via LPBF were investigated using an experimental framework based on mechanical testing and dislocation structure investigation. Manufacturing was performed using as-received and reused powder batches and the mechanical properties were compared to those of a conventionally casted material. The major conclusions are listed as follows:

- Powder reuse has no effect on microstructure, average porosity and fatigue properties with high plastic strain magnitude; and no significant influence on fatigue properties (LCF and MCF). In high cycle fatigue, an increase in fatigue life for reused powder samples is observed but not be explained by porosity analysis in X-Ray tomography.
- For similar plastic strain amplitudes in fatigue, LPBF samples exhibit larger stress amplitude but significantly reduced fatigue life (one order of magnitude) compared to cast due to the remaining presence of pores with diameter larger than 20 µm.
- Cyclic softening occurs for LPBF Ni20Cr since the microplasticity regime despite planar glide character. No softening occurs in the case of cast Ni20Cr.
- Softening in LCF- and MCF-LPBF specimens is mainly associated to back stress related to a modification of the initial dislocation cell structures inherited from LPBF process.
- The change in dislocation structure is initiated from the activation of slip systems for stresses lower than the yield stress due to probable dislocation sources located in the dendrite walls.
- This investigation confirms, hence, the role played by dislocation cells inherited from the LPBF process on the plastic behaviour independently of the monotonic or cyclic character of the mechanical loadings.

Nevertheless, there are a few limitations in this study that could be addressed in future research. First, other factors like precipitates or oxides at the dendritic walls or meltpool boundaries formed during LPBF process, might also govern the fatigue lifetime by influencing crack initiation and propagation under varied loading conditions. Such factors could be influential when porosity is further restricted by further optimising the LPBF process parameters. Oxides seem to be incoherent in nature with the FCC Ni-Cr matrix and this could create decohesion at the oxide-matrix interface resulting in fatigue fracture. Following the extensive high temperature applications of Ni alloys in the industry, further high temperature fatigue analysis of LPBF Ni20Cr is a promising prospect.

6. Acknowledgement

The Labex EMC3 is greatly acknowledged for the financial support of the Nichrofab project.

7. References

[1] B. Blakey-Milner *et al.*, "Metal additive manufacturing in aerospace: A review," *Materials & Design*, vol. 209, p. 110008, Nov. 2021, doi: 10.1016/j.matdes.2021.110008.

[2] M. Srinivas and B. S. Babu, "A Critical Review on Recent Research Methodologies in Additive Manufacturing," *Materials Today: Proceedings*, vol. 4, no. 8, pp. 9049–9059, Jan. 2017, doi: 10.1016/j.matpr.2017.07.258.

[3] B. Song, S. Dong, P. Coddet, H. Liao, and C. Coddet, "Fabrication of NiCr alloy parts by selective laser melting: Columnar microstructure and anisotropic mechanical behavior," *Materials & Design*, vol. 53, pp. 1–7, Jan. 2014, doi: 10.1016/j.matdes.2013.07.010.

[4] G. J. Gibbons, Ed., *Additive Manufacturing of Metals*. MDPI - Multidisciplinary Digital Publishing Institute, 2021. doi: 10.3390/books978-3-0365-0699-9.

[5] P. Moghimian *et al.*, "Metal Powders in Additive Manufacturing: A Review on Reusability and Recyclability of Common Titanium, Nickel and Aluminum Alloys," *Additive Manufacturing*, p. 102017, May 2021, doi: 10.1016/j.addma.2021.102017.

[6] T. DebRoy *et al.*, "Additive manufacturing of metallic components – Process, structure and properties," *Progress in Materials Science*, vol. 92, pp. 112–224, Mar. 2018, doi: 10.1016/j.pmatsci.2017.10.001.

[7] R. Cunningham, S. P. Narra, C. Montgomery, J. Beuth, and A. D. Rollett, "Synchrotron-Based X-ray Microtomography Characterization of the Effect of Processing Variables on Porosity Formation in Laser Power-Bed Additive Manufacturing of Ti-6Al-4V," *JOM*, vol. 69, no. 3, pp. 479–484, Mar. 2017, doi: 10.1007/s11837-016-2234-1.

[8] M. Kahlin *et al.*, "Improved fatigue strength of additively manufactured Ti6Al4V by surface post processing," *International Journal of Fatigue*, vol. 134, p. 105497, May 2020, doi: 10.1016/j.ijfatigue.2020.105497.

[9] K. Darvish, Z. W. Chen, and T. Pasang, "Reducing lack of fusion during selective laser melting of CoCrMo alloy: Effect of laser power on geometrical features of tracks," *Materials & Design*, vol. 112, pp. 357–366, Dec. 2016, doi: 10.1016/j.matdes.2016.09.086.

[10] P. D. Nezhadfar, S. Thompson, A. Saharan, N. Phan, and N. Shamsaei, "Structural integrity of additively manufactured aluminum alloys: Effects of build orientation on microstructure, porosity, and fatigue behavior," *Additive Manufacturing*, vol. 47, p. 102292, Nov. 2021, doi: 10.1016/j.addma.2021.102292.

[11] D. B. Witkin, D. Patel, T. V. Albright, G. E. Bean, and T. McLouth, "Influence of surface conditions and specimen orientation on high cycle fatigue properties of Inconel 718 prepared by laser

powder bed fusion," *International Journal of Fatigue*, vol. 132, p. 105392, Mar. 2020, doi: 10.1016/j.ijfatigue.2019.105392.
[12] M. M. Parvez, T. Pan, Y. Chen, S. Karnati, J. W. Newkirk, and F. Liou, "High Cycle Fatigue Performance of LPBF 304L Stainless Steel at Nominal and Optimized Parameters," *Materials*, vol. 13, no. 7, Art. no. 7, Jan. 2020, doi: 10.3390/ma13071591.
[13] K. Malekipour, M. Badrossamay, and M. Mashayekhi, "Parametric investigation of micro-pores coalescence in the microstructure of LPBF manufactured AISI 316 stainless steel under high cycle fatigue loading," *Engineering Failure Analysis*, vol. 144, p. 106942, Feb. 2023, doi: 10.1016/j.engfailanal.2022.106942.
[14] Z. Qin *et al.*, "Anisotropic high cycle fatigue property of Sc and Zr-modified Al-Mg alloy fabricated by laser powder bed fusion," *Additive Manufacturing*, vol. 49, p. 102514, Jan. 2022, doi: 10.1016/j.addma.2021.102514.
[15] G. Brot *et al.*, "Designing very high-cycle fatigue specimens of additively manufactured Ti-6Al-4V with different porosities and microstructures," *Procedia Structural Integrity*, vol. 38, pp. 604–610, Jan. 2022, doi: 10.1016/j.prostr.2022.03.062.
[16] F. Abroug, A. Monnier, L. Arnaud, Y. Balcaen, and O. Dalverny, "High cycle fatigue strength of additively manufactured AISI 316L Stainless Steel parts joined by laser welding," *Engineering Fracture Mechanics*, vol. 275, p. 108865, Nov. 2022, doi: 10.1016/j.engfracmech.2022.108865.
[17] E. Paccou *et al.*, "Investigations of powder reusing on microstructure and mechanical properties of Inconel 718 obtained by additive manufacturing," *Materials Science and Engineering: A*, vol. 828, p. 142113, Nov. 2021, doi: 10.1016/j.msea.2021.142113.
[18] H. Zhang, C. Li, Y. Shi, G. Yao, and Y. Zhang, "Fatigue and tensile deformation behaviors of laser powder bed fused 304L austenitic stainless steel," *Materials Science and Engineering: A*, vol. 849, p. 143503, Aug. 2022, doi: 10.1016/j.msea.2022.143503.
[19] A. Piglione *et al.*, "On the constitutive relationship between solidification cells and the fatigue behaviour of IN718 fabricated by laser powder bed fusion," *Additive Manufacturing*, vol. 47, p. 102347, Nov. 2021, doi: 10.1016/j.addma.2021.102347.
[20] M. Jin, E. Hosseini, Stuart. R. Holdsworth, and M.-S. Pham, "Thermally activated dependence of fatigue behaviour of CrMnFeCoNi high entropy alloy fabricated by laser powder-bed fusion," *Additive Manufacturing*, vol. 51, p. 102600, Mar. 2022, doi: 10.1016/j.addma.2022.102600.
[21] A. Gupta, C. J. Bennett, and W. Sun, "An experimental investigation on the progressive failure of an additively manufactured Laser Powder Bed Fusion Ti-6Al-4V aero-engine bracket under Low Cycle Fatigue," *Engineering Failure Analysis*, vol. 139, p. 106455, Sep. 2022, doi: 10.1016/j.engfailanal.2022.106455.
[22] J. Nguejio *et al.*, "Combined effect of a spread powder particle size distribution, surface machining and stress-relief heat treatment on microstructure, tensile and fatigue properties of 316L steel manufactured by laser powder bed fusion," *Int J Adv Manuf Technol*, Feb. 2023, doi: 10.1007/s00170-023-11008-w.
[23] G. Marnier, C. Keller, and L. Taleb, "Tensile prestrain memory effect on subsequent cyclic behavior of FCC metallic materials presenting different dislocations slip modes," *International Journal of Plasticity*, vol. 78, pp. 64–83, Mar. 2016, doi: 10.1016/j.ijplas.2015.11.001.
[24] S. S. Joshi, C. Keller, L. Mas, W. Lefebvre, E. Hug, and J.-P. Couzinie, "On the origin of the strain hardening mechanisms of Ni20Cr alloy manufactured by laser powder bed fusion," *International Journal of Plasticity*, vol. 165, p. 103610, Jun. 2023, doi: 10.1016/j.ijplas.2023.103610.
[25] S. Murakami, M. Kawai, and Y. Ohmi, "Effects of Amplitude-History and Temperature-History on Multiaxial Cyclic Behavior of Type 316 Stainless Steel," *Journal of Engineering Materials and Technology*, vol. 111, no. 3, pp. 278–285, Jul. 1989, doi: 10.1115/1.3226467.
[26] C. E. Feltner and C. Laird, "Cyclic stress-strain response of F.C.C. metals and alloys—I Phenomenological experiments," *Acta Metallurgica*, vol. 15, no. 10, pp. 1621–1632, Oct. 1967, doi: 10.1016/0001-6160(67)90137-X.

[27] X. H. An, S. D. Wu, Z. G. Wang, and Z. F. Zhang, “Significance of stacking fault energy in bulk nanostructured materials: Insights from Cu and its binary alloys as model systems,” *Progress in Materials Science*, vol. 101, pp. 1–45, Apr. 2019, doi: 10.1016/j.pmatsci.2018.11.001.
[28] S. R. Agnew and J. R. Weertman, “Cyclic softening of ultrafine grain copper,” *Materials Science and Engineering: A*, vol. 244, no. 2, pp. 145–153, Apr. 1998, doi: 10.1016/S0921-5093(97)00689-8.
[29] C. Keller, G. Marnier, W. Veloz, and L. Taleb, “Influence of the stacking fault energy and temperature on the prestrain memory effect of face centered cubic metal submitted to cyclic loadings,” *MATEC Web Conf.*, vol. 165, p. 06008, 2018, doi: 10.1051/matecconf/201816506008.
[30] E. Hug, M. Lelièvre, C. Folton, A. Ribet, M. Martinez-Celis, and C. Keller, “Additive manufacturing of a Ni-20 wt%Cr binary alloy by laser powder bed fusion: Impact of the microstructure on the mechanical properties,” *Materials Science and Engineering: A*, vol. 834, p. 142625, Feb. 2022, doi: 10.1016/j.msea.2022.142625.
[31] G. Marnier, “Etude des effets de mémoire de pré-écrouissage affectant le comportement mécanique cyclique de matériaux métalliques présentant différents modes de glissement des dislocations,” p. 231.
[32] C.-S. Yun, T. Hanawa, M.-H. Hong, B. K. Min, and T.-Y. Kwon, “Biocompatibility of Ni–Cr alloys, with the same composition, prepared by two new digital manufacturing techniques,” *Materials Letters*, vol. 305, p. 130761, Dec. 2021, doi: 10.1016/j.matlet.2021.130761.
[33] S. Das, J. B. Seol, Y. C. Kim, and C. G. Park, “Structure and mechanical properties of Ni–Cr alloy produced by single roll strip casting,” *Materials & Design*, vol. 31, no. 1, pp. 570–573, Jan. 2010, doi: 10.1016/j.matdes.2009.07.006.
[34] N. R. Dudova and R. O. Kaibyshev, “Short-range ordering and mechanical properties of a Ni-20%Cr alloy,” *J. Phys.: Conf. Ser.*, vol. 240, p. 012081, Jul. 2010, doi: 10.1088/1742-6596/240/1/012081.
[35] X. Feaugas and C. Gaudin, “Ratchetting process in the stainless steel AISI 316L at 300 K: an experimental investigation,” *International Journal of Plasticity*, vol. 20, no. 4, pp. 643–662, Apr. 2004, doi: 10.1016/S0749-6419(03)00076-7.
[36] S. S. Yadav, S. C. Roy, and S. Goyal, “A comprehensive review and analysis of Masing/non-Masing behavior of materials under fatigue,” *Fatigue & Fracture of Engineering Materials & Structures*, vol. n/a, no. n/a, doi: 10.1111/ffe.13906.
[37] J. Colin, A. Fatemi, and S. Taheri, “Cyclic hardening and fatigue behavior of stainless steel 304L,” *Journal of Materials Science*, vol. 46, pp. 145–154, Sep. 2011, doi: 10.1007/s10853-010-4881-x.
[38] M. Jambor, T. Vojtek, P. Pokorný, and M. Šmíd, “Effect of Solution Annealing on Fatigue Crack Propagation in the AISI 304L TRIP Steel,” *Materials*, vol. 14, no. 6, Art. no. 6, Jan. 2021, doi: 10.3390/ma14061331.
[39] M. S. Pham, C. Solenthaler, K. G. F. Janssens, and S. R. Holdsworth, “Dislocation structure evolution and its effects on cyclic deformation response of AISI 316L stainless steel,” *Materials Science and Engineering: A*, vol. 528, no. 7, pp. 3261–3269, Mar. 2011, doi: 10.1016/j.msea.2011.01.015.
[40] T. Mayer, E. Mazza, and S. R. Holdsworth, “Parameter evolution in a continuous Masing approach for cyclic plasticity and its physical interpretation,” *Mechanics of Materials*, vol. 57, pp. 86–96, Feb. 2013, doi: 10.1016/j.mechmat.2012.10.014.
[41] T. Mayer, E. Mazza, and S. R. Holdsworth, “A continuous Masing approach for a physically motivated formulation of temperature and strain-rate dependent plasticity,” *International Journal of Pressure Vessels and Piping*, vol. 102–103, pp. 1–12, Feb. 2013, doi: 10.1016/j.ijpvp.2012.11.001.
[42] H. Mughrabi and H.-J. Christ, “Cyclic Deformation and Fatigue of Selected Ferritic and Austenitic Steels: Specific Aspects,” *ISIJ International*, vol. 37, no. 12, pp. 1154–1169, 1997, doi: 10.2355/isijinternational.37.1154.
[43] M. S. Pham, S. R. Holdsworth, K. G. F. Janssens, and E. Mazza, “Cyclic deformation response of AISI 316L at room temperature: Mechanical behaviour, microstructural evolution, physically-

based evolutionary constitutive modelling," *International Journal of Plasticity*, vol. 47, pp. 143–164, Aug. 2013, doi: 10.1016/j.ijplas.2013.01.017.
[44] A. Plumtree and H. A. Abdel-Raouf, "Cyclic stress–strain response and substructure," *International Journal of Fatigue*, vol. 23, no. 9, pp. 799–805, Oct. 2001, doi: 10.1016/S0142-1123(01)00037-8.
[45] S. Goyal *et al.*, "Low Cycle Fatigue and Cyclic Plasticity Behavior of Indian PHWR/AHWR Primary Piping Material," *Procedia Engineering*, vol. 55, pp. 136–143, Jan. 2013, doi: 10.1016/j.proeng.2013.03.232.
[46] N. Khutia, P. P. Dey, S. K. Paul, and S. Tarafder, "Development of non Masing characteristic model for LCF and ratcheting fatigue simulation of SA333 C–Mn steel," *Mechanics of Materials*, vol. 65, pp. 88–102, Oct. 2013, doi: 10.1016/j.mechmat.2013.05.016.
[47] R. R. Dehoff, M. M. Kirka, F. A. List, K. A. Unocic, and W. J. Sames, "Crystallographic texture engineering through novel melt strategies via electron beam melting: Inconel 718," *Materials Science and Technology*, vol. 31, no. 8, pp. 939–944, Jun. 2015, doi: 10.1179/1743284714Y.0000000697.
[48] J. Berez and C. Saldana, "Fatigue of laser powder bed fusion processed 17-4 stainless steel using prior process exposed powder feedstock," *Journal of Manufacturing Processes*, vol. 71, pp. 515–527, Nov. 2021, doi: 10.1016/j.jmapro.2021.09.045.
[49] S. S. Yadav, S. C. Roy, J. Veerababu, and S. Goyal, "Quantitative Assessment and Analysis of Non-Masing Behavior of Materials under Fatigue," *J. of Materi Eng and Perform*, vol. 30, no. 3, pp. 2102–2112, Mar. 2021, doi: 10.1007/s11665-021-05494-w.
[50] J. Fumfera, J. Džugan, J. Kuželka, R. Procházka, and M. Španiel, "Strain-amplitude dependent cyclic hardening of 08Ch18N10T austenitic stainless steel," *IOP Conf. Ser.: Mater. Sci. Eng.*, vol. 179, no. 1, p. 012026, Feb. 2017, doi: 10.1088/1757-899X/179/1/012026.
[51] L. Cui, F. Jiang, R. L. Peng, R. T. Mousavian, Z. Yang, and J. Moverare, "Dependence of microstructures on fatigue performance of polycrystals: A comparative study of conventional and additively manufactured 316L stainless steel," *International Journal of Plasticity*, vol. 149, p. 103172, Feb. 2022, doi: 10.1016/j.ijplas.2021.103172.
[52] L. Cui *et al.*, "Cyclic response of additive manufactured 316L stainless steel: The role of cell structures," *Scripta Materialia*, vol. 205, p. 114190, Dec. 2021, doi: 10.1016/j.scriptamat.2021.114190.
[53] A. Sola and A. Nouri, "Microstructural porosity in additive manufacturing: The formation and detection of pores in metal parts fabricated by powder bed fusion," *Journal of Advanced Manufacturing and Processing*, vol. 1, no. 3, p. e10021, 2019, doi: 10.1002/amp2.10021.
[54] B. M. Morrow *et al.*, "Impact of Defects in Powder Feedstock Materials on Microstructure of 304L and 316L Stainless Steel Produced by Additive Manufacturing," *Metall Mater Trans A*, vol. 49, no. 8, pp. 3637–3650, Aug. 2018, doi: 10.1007/s11661-018-4661-9.
[55] M. Åsberg, G. Fredriksson, S. Hatami, W. Fredriksson, and P. Krakhmalev, "Influence of post treatment on microstructure, porosity and mechanical properties of additive manufactured H13 tool steel," *Materials Science and Engineering: A*, vol. 742, pp. 584–589, Jan. 2019, doi: 10.1016/j.msea.2018.08.046.
[56] T. Voisin *et al.*, "Defects-dictated tensile properties of selective laser melted Ti-6Al-4V," *Materials & Design*, vol. 158, no. C, Art. no. LLNL-JRNL-741649, Aug. 2018, doi: 10.1016/j.matdes.2018.08.004.
[57] C. Panwisawas, C. L. Qiu, Y. Sovani, J. W. Brooks, M. M. Attallah, and H. C. Basoalto, "On the role of thermal fluid dynamics into the evolution of porosity during selective laser melting," *Scripta Materialia*, vol. Complete, no. 105, pp. 14–17, 2015, doi: 10.1016/j.scriptamat.2015.04.016.
[58] J. N. D. Ngnekou *et al.*, "Fatigue properties of AlSi10Mg produced by Additive Layer Manufacturing," *International Journal of Fatigue*, vol. 119, pp. 160–172, Feb. 2019, doi: 10.1016/j.ijfatigue.2018.09.029.

[59] V. Prithivirajan and M. D. Sangid, “The role of defects and critical pore size analysis in the fatigue response of additively manufactured IN718 via crystal plasticity,” *Materials & Design*, vol. 150, pp. 139–153, Jul. 2018, doi: 10.1016/j.matdes.2018.04.022.
[60] P. Pant *et al.*, “A study of the influence of novel scan strategies on residual stress and microstructure of L-shaped LPBF IN718 samples,” *Materials & Design*, vol. 214, p. 110386, Feb. 2022, doi: 10.1016/j.matdes.2022.110386.
[61] P. Sandmann *et al.*, “Influence of laser shock peening on the residual stresses in additively manufactured 316L by Laser Powder Bed Fusion: A combined experimental–numerical study,” *Additive Manufacturing*, vol. 60, p. 103204, Dec. 2022, doi: 10.1016/j.addma.2022.103204.
[62] Y. Li and C. Laird, “Cyclic response and dislocation structures of AISI 316L stainless steel. Part 2: polycrystals fatigued at intermediate strain amplitude,” *Materials Science and Engineering: A*, vol. 186, no. 1–2, pp. 87–103, Oct. 1994, doi: 10.1016/0921-5093(94)90307-7.
[63] X. Feaugas, “On the origin of the tensile flow stress in the stainless steel AISI 316L at 300 K: back stress and effective stress,” *Acta Materialia*, vol. 47, no. 13, pp. 3617–3632, Oct. 1999, doi: 10.1016/S1359-6454(99)00222-0.